Research Article

Computational Investigation of Mononuclear Iron Water Oxidation Catalyst Design

Kristal Stevens [1], Emily Jarvis [1,*]

[1]Department of Chemistry and Biochemistry, Loyola Marymount University, 1 LMU Drive, Los Angeles, CA 90045, United States.
Email: Emily.Jarvis@lmu.edu

Abstract: Hydrogen production from non-carbon sources is an essential component of clean and sustainable technology for reducing greenhouse gas emissions from fuels. Water oxidation, which splits water molecules into hydrogen (protons) and molecular oxygen, is a thermodynamically challenging, multistep reaction achieved in photosynthetic organisms via photocatalysis by the Oxygen Evolving Complex (OEC) of Photosystem II. Mononuclear water oxidation catalysts that aim to mimic nature typically rely on heavy, rare metals such as ruthenium and iridium. Replacing these metals with iron is particularly appealing because it is abundant, benign, and inexpensive. We use density functional theory to characterize the catalytic ability of mononuclear iron photocatalysts compared with their ruthenium counterparts for 20 different ligand modifications with varying degrees of electron withdrawing behavior. We quantify the energetics, bond lengths, and charges in each of the steps leading to the highest oxidation state of the metal and necessary O-O bond formation in a mechanism determined experimentally for ruthenium catalysts and in many ways analogous to that followed by the OEC. Although many of the iron catalysts exhibited prohibitively high redox potentials in achieving the highest oxidation state required by this mechanism, a few display promising energetics and stability at each step explored. These results provide insights regarding the feasibility and performance of water oxidation catalysts using earth abundant metals as well as pinpointing mechanistic steps where catalytic ability degrades.

Keywords: water oxidation, density functional theory, mononuclear iron catalyst, computational chemistry

1. Introduction

Improving renewable energy technologies and implementation is essential for reducing greenhouse gas emissions. In addition to the harmful environmental impact, obtaining power from burning fossil fuels is limited by finite resources as well as thermodynamic efficiency. Globally our answer to sustainable power likely will involve multiple solutions including solar, wind, nuclear, and hydrogen fuel to replace carbon-based energy sources. Although in theory

hydrogen fuel is free of carbon, in current practice, hydrogen fuel is mainly produced through steam methane reforming using light hydrocarbons [1]. Electrolysis produces hydrogen through water splitting but is energetically costly. Alternatively, splitting water through photocatalysis ideally could be achieved using sunlight and would produce stored solar power in the form of hydrogen fuel. The half reaction for this oxidation is shown with the tabulated potential of -1.23 V relative to the Normal Hydrogen Electrode (NHE) 0.00 V (Equation 1).

$$H_2O \rightarrow 2H^+ + 2e^- + \frac{1}{2}O_2 \quad E^o = -1.23 \text{ V} \tag{1}$$

Non-potable water is inexpensive, abundant, and carbon-free, making it an ideal source from which to obtain hydrogen fuel despite its thermodynamic challenges.

Water oxidation is routinely achieved in all photosynthetic organisms through photocatalysis. In nature, the oxygen evolving complex (OEC) of Photosystem II (PSII) employs a catalyst consisting of four neighboring manganese sites for oxidizing water [2]. The cage-like structure of the OEC allows the four manganese to share the redox demands of the photocatalyst, such that none of the sites need to cycle above a +4 oxidation state. Many promising synthetic water oxidation catalysts (WOCs) also employ more than one metal site to share the burden of the redox cycling in the oxidation mechanism. For example, Nocera et al. have made significant contributions towards developing the Artificial Leaf which employs a cobalt phosphate cluster (Co-OEC) to drive water oxidation [3]. Despite such advancements for polynuclear WOCs, the order of oxidation events and absolute oxidation state for each manganese site that occur over the oxidation mechanism for PSII is very challenging to determine [4]. Our present study focuses on mononuclear catalyst design allowing confident assignment of the single metal site oxidation state. This approach provides simpler mechanistic analysis, which allows us to gain general behavior insights even though optimal working catalysts may have more than one metal site.

Ruthenium mononuclear WOCs are very successful in terms of turnover number and energetics, but these catalysts have the notable disadvantage of containing an expensive, rare metal that is environmentally destructive to procure. We wish to develop efficient WOCs based on abundant and environmentally benign first-row transition metals [5]. Iron is particularly interesting due to its earth abundance and since it is in the same group as ruthenium, positioned directly above it on the periodic table. Progress has been made with several mononuclear Fe based WOCs [6-8]. Unfortunately, these catalysts are less efficient and less stable than ruthenium based WOCs, often requiring highly acidic conditions and not exhibiting mononuclear mechanistic behavior despite the molecular structure. Advancing mononuclear Fe WOC design is crucial to develop useful catalysts for large-scale conversion of non-potable water into hydrogen fuel and provide broad insights into catalyst design.
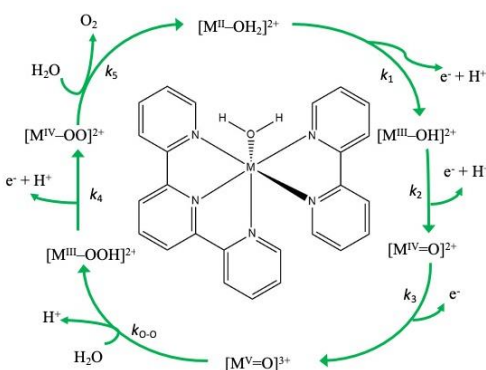
Figure 1. Mononuclear ruthenium catalyst water oxidation mechanism as proposed by Chen and coworkers [10]. We applied this same mechanism across all our proposed catalysts investigated here. A representative catalyst structure where M = Ru or Fe is shown in the center and is represented as $[MII-OH_2]^{2+}$. The charge, the oxidation state on the metal, and the attached water or other species for the points along the mechanism is represented.

Here, we computationally investigate 20 mononuclear catalysts for iron and compare to analogous ruthenium complexes, some of which have been explored experimentally and in our prior study [9]. To pinpoint mechanistic steps where catalytic ability degrades and improve Fe WOC design, we strategically manipulate the ligands of our catalyst series by varying the electron donating and electron withdrawing character. Then, we analyze the energetic,

electronic, and structural properties of each catalyst at each step along a mechanism originally proposed for mononuclear ruthenium photocatalysts, which in many ways follows the mechanism of water oxidation for the OEC in PSII except that the redox steps are required of a single metal center as opposed to the shared redox burden across the four manganese in the OEC (Figure 1) [10]. For an up-to-date review on ligand modification for mononuclear water splitting catalysts, refer to a recent comprehensive review and references therein [11].

2. Materials and Methods

We perform density functional theory (DFT) calculations using the B3LYP exchange-correlation functional [12] employing the LanL2DZ basis set with accompanying effective core potential for iron and ruthenium [13] and with the accompanying D95V basis for first row elements. These particular functional and basis set choices are similar to those employed in our prior study and vetted more extensively there to ensure our computed values reflected known experimental and other computed values [9]. We included the effect of water solvation using the integral equation formalism variant of a polarizable continuum model (IEFPCM) [14, 15] as implemented within the Gaussian 16 computational chemistry software [16]. We optimized the geometries of each structure with the IEFPCM present throughout the optimization. We tested several of the lowest spin states and chose the energetically lowest state for subsequent analysis. Our optimization and thermodynamic free energy calculations did not impose symmetry or restrict spin states. Mulliken populations were analyzed to give a qualitative measure of local bonding around the metal centers and observe trends in bonding behavior [17].

The oxidation potentials were calculated by relating the calculated standard Gibbs energy of the reduction in solvent (ΔG^o) with the voltage through the well-known Equation 2:

$$-nFE^o = \Delta G^o \tag{2}$$

with F the Faraday constant and n the number of electrons involved in the oxidation step. For comparison to experimental values, these E^o were referenced to the NHE, which was corrected by 59 mV for the changing pH conditions in the proton-coupled-electron-transfer steps of the mechanism since those include the complex releasing a proton to solution. Our goal is not to predict the voltages of the redox couples but to ensure that our calculations capture enough of the pertinent physics to meaningfully investigate the intramolecular variations from one catalyst to the next. Our oxidation values were modified by using a linear fit to coincide better with experimentally measured values using a method detailed in our prior study of ruthenium catalysts and by others [9, 18]. Although ionization energies and electron affinities can be calculated quite accurately within DFT, the relevant redox potentials are more challenging. This can be attributed to the additional complexity of these values in experimental measures as well as the particular choices within the computational approach including features of the water solvent, whether dynamics are included, and details of the ab initio approach [19]. The proton-coupled-electron-transfer steps of the mechanism are anticipated to be most sensitive to the details of these choices. Of course, there is no meaningful electronic structure energy when no electron is present on the proton. Here, we use a value for the solvated proton free energy of -272.2 kcal/mol previously employed by ourselves and others [9, 18, 20].

An essential step in the water oxidation mechanism involves the O-O bond forming step from the [MV=O]3+ state with the rate constant k_{o-o} shown in Figure 1. This step had been explored dynamically for some ruthenium catalysts by Chen *et al*. employing Quantum Mechanics/Molecular Mechanics (QM/MM) simulations using a TIP3P water model for all water molecules except the two water molecules included in the QM portion [21]. Our calculations for this portion of the mechanism included geometry optimizations with only the two explicit QM water molecules as well as the IEFPCM implicit water solvent [9]. These calculations resulted in similar reactant/product structures to those observed in the QM/MM calculations for the catalysts we investigated in common.

3. Results and Discussion

We computationally explored 20 mononuclear catalysts for iron and compared to analogous ruthenium complexes. We varied their tridentate and/or bidentate ligands to tune the electronic structure of the catalyst and impact its reactivity. Eleven of these mononuclear ruthenium catalysts were investigated in our prior study employing similar computational methods. Previously, most of those ruthenium catalysts had been characterized experimentally by

others for catalytic performance including turnover frequency by monitoring oxygen evolution and by using cyclic voltammetry to elucidate the electrochemical steps of the catalytic water oxidation mechanism. Our prior paper discusses these values and quantifies the extent to which our computational approach captures these trends [9]. Wishing to explore the impact of electron donating and withdrawing groups more methodically, some of the additional catalysts included in our current study were inspired by Watabe et al. to scan a range of substituents on the tridentate ligand ordered according to Hammett constants [22]. Hence, here we numerically ordered the twenty catalysts by increasing electron donating ability of the substituents as well as increasing nitrogen content of the ligands to aid in observing trends across these series, resulting in our catalysts labeled 1-20. Figure 2 shows these ligands, which all bond through nitrogen atoms except in the case of bidentate ligands shown in F and G (catalysts 14, 15, 16, 19) which bond through a carbon atom in the axial position. Table 1 displays the specific ligand pairings from those structures shown in Figure 2 as well as the common shorthand nomenclature (tpy = 2,2′:6′2″-terpyridine, bpy = 2,2′-bipyridine, bpm = 2,2'-bipyrimidine, ttz = 2,2′:4′,2″-ter-1-3-5-triazine, Mebimpy = 2,6-bis(1-methylbenzimidazol-2-yl)pyridine, Mebim-py = 3-methyl-1-pyridylbenzimidazol-2-ylidene, Mebim-pz = 3-methyl-1-pyrazylbenzimidazol-2-ylidene. Me = methyl, MeO = methoxy, EtO = ethoxy, PrO = propoxy) for each of these 20 catalysts.

Table 1. Description and short-hand naming of catalysts with letters referring to the ligand structures shown in Figure 2. M = Fe or Ru

Catalyst	Combined Structures	Naming Shorthand
1	A and D with H for A-R and D-R	$[M(tpy)(bpy)(OH_2)]^{2+}$
2	A and D with Cl for A-R and H for D-R	$[M(tpy\text{-}Cl)(bpy)(OH_2)]^{2+}$
3	A and D with Me for A-R and H for D-R	$[M(tpy\text{-}Me)(bpy)(OH_2)]^{2+}$
4	A and D with EtO for A-R and H for D-R	$[M(tpy\text{-}OEt)(bpy)(OH_2)]^{2+}$
5	A and D with PrO for A-R and H for D-R	$[M(tpy\text{-}PrO)(bpy)(OH_2)]^{2+}$
6	A and D with MeO for A-R and H for D-R	$[M(tpy\text{-}OMe)(bpy)(OH_2)]^{2+}$
7	A and D with OH for A-R and H for D-R	$[M(tpy\text{-}OH)(bpy)(OH_2)]^{2+}$
8	A and D with Me$_2$N for A-R and H for D-R	$[M(tpy\text{-}Me_2N)(bpy)(OH_2)]^{2+}$
9	A and D with MeO for A-R and D-R	$[M(tpy\text{-}OMe)(bpy\text{-}OMe)(OH_2)]^{2+}$
10	A and D with COOH for A-R and D-R	$[M(tpy\text{-}COOH)(bpy\text{-}COOH)(OH_2)]^{2+}$
11	A and D with Cl for A-R and D-R	$[M(tpy\text{-}Cl)(bpy\text{-}Cl)(OH_2)]^{2+}$
12	A and D with NH$_2$ for A-R and D-R	$[M(tpy\text{-}NH_2)(bpy\text{-}NH_2)(OH_2)]^{2+}$
13	A and E with H for A-R	$[M(tpy)(bpm)(OH_2)]^{2+}$
14	A and G with H for A-R	$[M(tpy)(Mebim\text{-}pz)(OH_2)]^{2+}$
15	A and F with H for A-R	$[M(tpy)(Mebim\text{-}py)(OH_2)]^{2+}$
16	A and F with Cl for A-R	$[M(tpy\text{-}Cl)(Mebim\text{-}py)(OH_2)^{2+}$
17	C and E	$[M(Mebimpy)(bpm)(OH_2)]^{2+}$
18	B and E	$[M(ttz)(bpm)(OH_2)]^{2+}$
19	B and F	$[M(ttz)(Mebim\text{-}py)(OH_2)]^{2+}$
20	B and D with Cl for D-R	$[M(ttz)(bpy\text{-}Cl)(OH_2)]^{2+}$
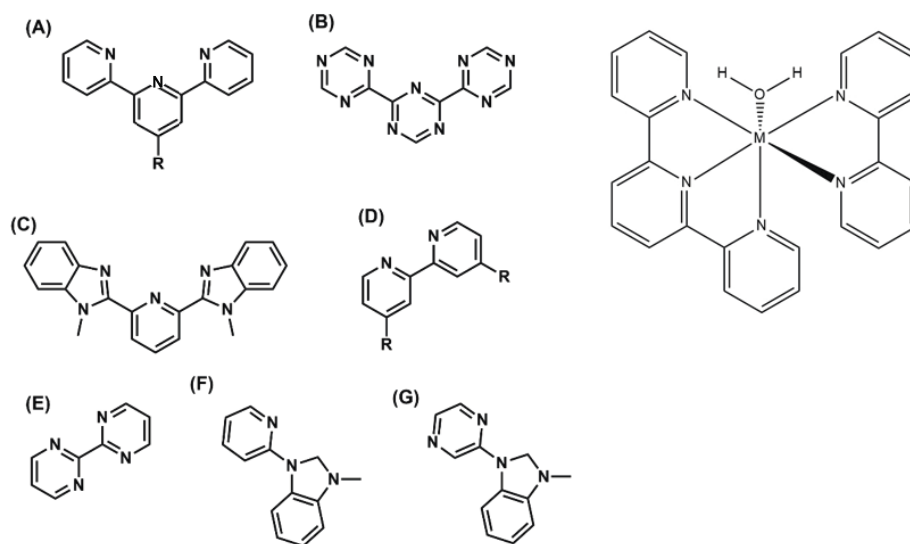
Figure 2. Visual showing the combinations of bidentate and tridentate ligands surrounding the single metal center for the 20 iron and ruthenium catalysts enumerated in Table 1 with A) tpy = 2,2′:6′2″-terpyridine, B) ttz = 2,2′:4′,2″-ter-1-3-5-triazine, C) Mebimpy = 2,6-bis(1-methylbenzimidazol-2-yl)pyridine D) bpy = 2,2′-bipyridine, E) bpm = 2,2'-bipyrimidine F) Mebim-py = 3-methyl-1-pyridylbenzimidazol-2-ylidene and G) Mebim-pz = 3-methyl-1-pyrazylbenzimidazol-2-ylidene. The structure for a representative complex on the right represents the tridentate ligand (A), bidentate ligand (B), and a single water molecule bonded to the metal (M=Fe or Ru), in this case the [M(tpy)(bpy)(OH$_2$)]$^{2+}$.

We characterized the energetics of each catalyst from the starting point of the mechanism through each of the electrochemical steps leading to oxygen-oxygen (O-O) bond forming according to a well-studied water oxidation mechanism followed by some mononuclear ruthenium WOCs (Figure 1) [10]. Table 2 shows our fit calculated potentials for each catalyst at Fe(III)/Fe(II), Fe(IV)/Fe(III), and Fe(V)/Fe(IV) as well as the energetic barrier (the Gibb's free energy difference between reactants and products), which has been show to essentially capture the barrier for this concerted proton transfer reaction in the critical O-O bond forming step [21, 23]. Table 3 shows these values for ruthenium as the metal center instead of iron. Eleven of these were reported in more detail in our prior study [9] and included in Table 3 for ease of comparison to the added Ru and novel Fe catalysts explored in this study.

Table 2. Summary of calculated electrochemical voltages for stepwise oxidation of Fe in the catalyst from II to V for steps leading to Fe^V and the change in ΔG (k_{o-o}), with catalyst variations numbered as detailed in Table 1.

Catalyst	E (III/II)	E (IV/III)	E (V/IV)	ΔΔG (kcal/mol)
1	0.91	1.19	2.01	12.7
2	0.93	1.19	2.04	15.8
3	0.90	1.16	2.00	13.9
4	0.92	1.18	2.00	16.9
5	0.90	1.19	2.00	14.8
6	0.92	1.18	2.01	16.8
7	0.90	1.18	2.09	14.3
8	0.87	1.16	1.59	15.3
9	0.89	1.18	2.05	17.5
10	0.93	1.14	2.14	13.4

11	0.95	1.21	2.12	13.7
12	0.86	1.13	1.68	15.9
13	0.96	1.20	2.01	15.2
14	0.98	1.20	2.01	18.5
15	0.95	1.21	1.93	19.0
16	0.96	1.22	1.82	18.6
17	0.96	1.21	1.74	14.6
18	1.14	1.21	2.33	10.1
19	1.23	1.13	1.87	11.4
20	1.24	1.10	2.26	7.9

Table 3. Summary of calculated electrochemical voltages for stepwise oxidation of Ru in the catalyst from II to V for steps leading to Ru^V and the change in ΔG ($k_{o\text{-}o}$), with catalyst variations numbered as detailed in Table 1. Catalysts 1, 4, 6, 9-11, 13-15, and 17-18 were included in our prior study [9].

| Catalyst	E (III/II)	E (IV/III)	E (V/IV)	$\Delta\Delta G$ (kcal/mol)
1	1.02	1.25	1.81	11.2
2	0.97	1.04	1.81	14.3
3	0.98	1.00	1.76	14.8
4	0.93	1.56	1.82	12.2
5	0.94	1.01	1.72	17.0
6	0.93	1.02	1.73	13.5
7	0.95	1.03	1.73	13.7
8	0.94	1.01	1.50	15.4
9	0.91	1.02	1.69	15.6
10	1.07	0.99	1.86	11.3
11	0.98	1.05	1.84	9.7
12	0.85	1.00	1.51	18.2
13	0.99	1.04	1.85	10.3
14	1.09	1.11	1.76	9.0
15	1.06	1.10	1.68	12.2
16	1.07	1.10	1.71	14.0
17	0.94	1.06	1.66	14.6
18	1.09	1.08	2.07	6.7
19	1.23	1.15	1.88	12.9
20	1.13	1.10	2.16	8.2

As expected, the Ru catalysts overall exhibited more favorable energetics relative to the Fe catalysts. Additionally, both metals followed similar trends: when redox potentials were high for Fe, they were also high for Ru and when low for Fe, also low for Ru. This suggests a functional Fe catalyst may follow the same or similar proposed mononuclear Ru water oxidation mechanism. We and others have noted previously for ruthenium that the most challenging steps in the mechanism involve achieving the M(V) formal oxidation state and overcoming the energetic barrier for the critical O-O bond forming step The general trend seen here and noted in prior studies is that these two most challenging steps are somewhat inversely proportional [9, 10]. The redox half-reaction M(V/IV) is where some catalysts for both Fe and Ru display potentials that are likely too high to be realized experimentally and/or would lead to rapid degradation of the catalyst. A general guideline in considering these potentials is that anything over 2.00 V would be too high for maintaining a robust catalyst and finding reasonable paired reduction half-reactions to drive such oxidations. Additionally for the energy barrier forming the O-O bond, computed values in the range of 10 kcal/mol or lower are promising, even though precise values are less relevant than insights from investigating trends across the catalysts here.

As mentioned, it is observed that many catalysts displaying high redox potentials to achieve the +5 state have corresponding lower energy barriers for the O-O bond forming step and vice versa. For instance, Fe and Ru catalysts 18 and 20 had high M(V/IV) redox potentials and a relatively low $\Delta\Delta G$ ($k_{o\text{-}o}$). Other catalysts like 8 and 12 for both Fe and Ru had relatively low M(V/IV) redox potentials and high $\Delta\Delta G$ ($k_{o\text{-}o}$). It seems likely that greater stability in the +5 oxidation state of the mononuclear catalyst leads to a more challenging O-O reaction barrier, which creates a somewhat delicate balance for optimal catalyst design.

Through strategic variation of the ligands, we were able to produce an iron catalyst that exhibited more favorable computed energetics than the corresponding ruthenium variant. This was catalyst 19 ($[M(ttz)(Mebim\text{-}py)(OH_2)]^{2+}$) where the M(V/IV) and $\Delta\Delta G$ (ko-o) for Fe was 1.87 V and 11.4 kcal/mol with the corresponding steps for Ru showing 1.88 V and 12.9 kcal/mol, respectively. This is an interesting catalyst because the tridentate ligand has an extreme level of nitrogen content to exaggerate that effect and the bidentate ligand has a carbon in the axial position that bonds to the metal. Catalyst 15 has the same bidentate ligand, but a different tridentate ligand (tpy) containing less nitrogen. This change made a significant difference in the computed energetics of the catalyst. For catalyst 15, the iron variant's energetics were markedly less favorable than ruthenium with an Fe(V/IV) of 1.93 V and $\Delta\Delta G$ ($k_{o\text{-}o}$) of 19 kcal/mol while the Ru catalyst displayed 1.68 V and 12.2 kcal/mol, respectively.

Even subtle differences in the ligands may have a strong influence on the energetics of the catalysts. How exactly these ligands and substituents achieve greater thermodynamic efficiency, particularly in light of the delicate balance between the two mechanistic steps on which we focus, is a challenge to elucidate. To investigate intramolecular features that provide some insight into the resulting energetics, we analyzed bond length and Mulliken charge data to highlight certain catalysts that exhibited the most extreme or unusual behavior.

As the catalyst cycles to higher oxidation states, bond lengths are subject to change. Of particular interest is the bond length between the metal and oxygen, representing the "active site" of the catalyst as well as the ligand bond opposite to this. Large changes in bond lengths in these axial positions of the octahedral complex can lead to higher redox potentials and point to the likelihood of catalytic degradation if the corresponding axial ligand bond is too weak. The Fe-O bond length differences (final minus initial Fe-O bond lengths across the mechanistic steps indicated) for Fe(III/II), Fe(IV/III), and Fe(V/IV) contract on average by 10.4%, 9.3%, and 0.63% relative to the initial bond lengths, respectively (Figure 3). The more dramatic bond contraction at the Fe(III/II) and Fe(IV/III) steps is expected since the O atom loses a proton at each of those mechanistic steps. The smaller bond difference at the Fe(V/IV) step is associated with only removing one electron from the Fe-O π^* orbital. Among all the catalysts, the Fe-O bonding differences, as quantified by associated bond length changes, are quite similar until they reach the Fe(V/IV) oxidation step. Catalysts 7, 10, 11, 14 and 15 have significantly large positive Fe-O bond length differences for the V/IV oxidation step, which corresponds with high (V/IV) redox potentials of 2.09, 2.14, 2.12, 2.01, and 1.93 V, respectively.
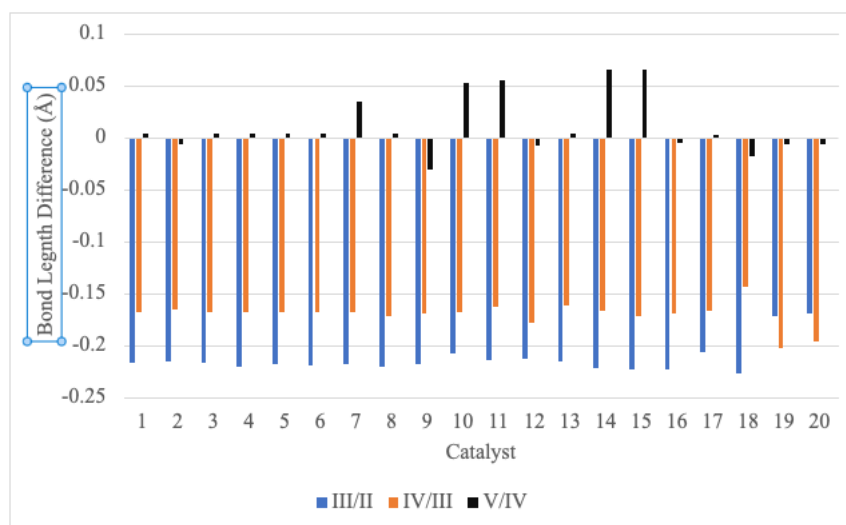
Figure 3. Fe-O bond length difference (final – initial) across mechanistic steps leading from Fe(II) to Fe(V).

Exploring the underlying features of the electron density on the metal and oxygen atom as the catalytic mechanism proceeds also can be a complimentary tool for understanding catalytic behavior. The Fe atom on catalysts 1-9, 11, 13, and 18 exhibited relatively consistent changes in electron density through the Fe(III/II) and Fe(IV/III) oxidation steps, while the other catalysts showed greater variability (Figure 4). Catalysts 10, 11, 14, and 15 had a large positive Mulliken charge difference on Fe for Fe(V/IV). This coincides with the large bond lengthening and high redox potentials at the Fe(V/IV) step mentioned in the previous paragraph. Catalyst 8 ([M(tpy-Me2N)(bpy)(OH2)]2+) had the smallest increase in charge on the Fe atom for the Fe(V/IV) step and had the lowest redox potential (1.59 V) out of all Fe catalysts.
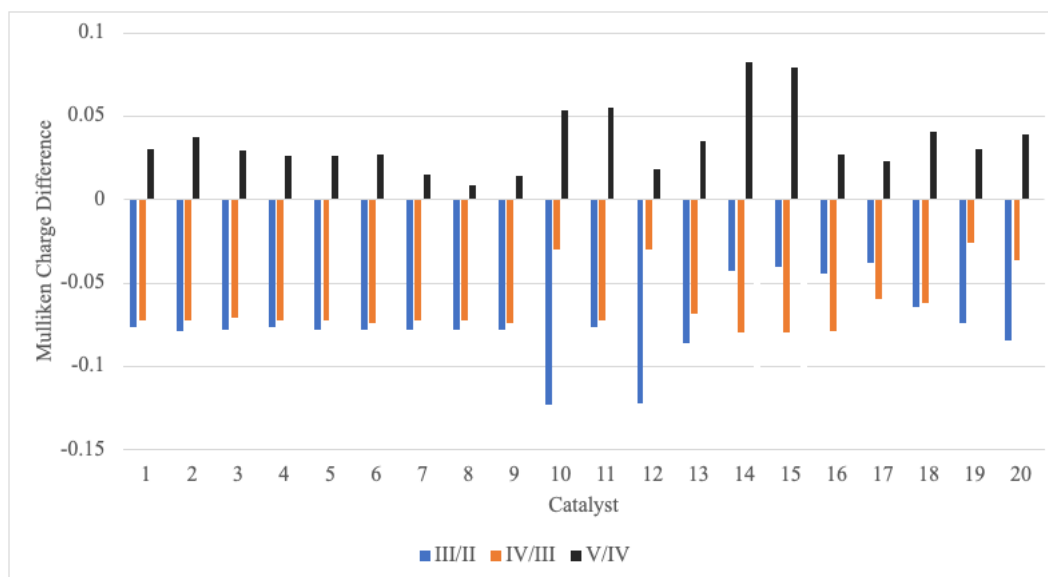
Figure 4. Mulliken Charge Differences on Fe along mechanistic steps leading from Fe(II) to Fe(V).

The Mulliken charge differences on the oxygen atom generally showed minor variations across the mechanism (with the sum of the first two redox steps showing broadly similar behavior) for all catalysts except 9, 10, 11, 14, and 15 at Fe(V/IV) (Figure 5). This also coincides with large bond lengthening and associated high redox potentials at the Fe(V/IV) step. There are, however, some exceptions where catalyst 7 has a large Fe(V/IV) bond lengthening and no

notable charge differences on Fe or O. Additionally, Catalyst 9 does not display unusual Fe(V/IV) bond length difference, but it has a significant positive Fe(V/IV) Mulliken charge change on O. These observations are attributed to differences in the electron donating or withdrawing ability of the ligands, where the catalysts are extremely sensitive at $[Fe^V=O]^{3+}$. We see that overall large changes in charge on the Fe atom and the O atom at Fe(V/IV) lead to higher oxidation potentials for that step and missing the corresponding low energy barrier for the O-O bond forming in most (except 10 and 11 where that barrier is relatively low).
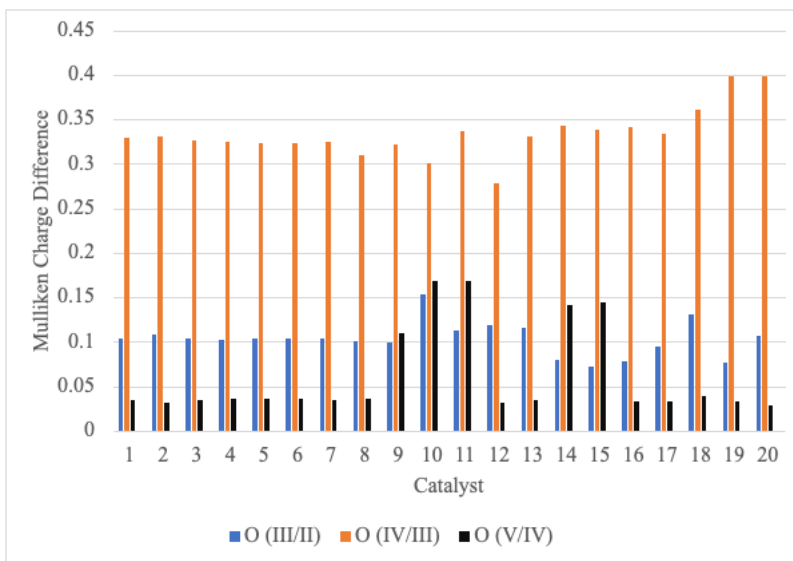
Figure 5. Mulliken Charge Differences on O along mechanistic steps leading from Fe (II) to Fe (V).

Figures 3-5 relate to the mechanistic steps where the catalyst cycles from a +II to a +V oxidation state on the metal center. The subsequent O−O bond-forming step is generally seen as the catalytic bottleneck and involves an O-atom attack on H_2O by $[M^V=O]^{3+}$ in concert with a proton transfer to neighboring water molecule [8, 21, 23]. Here, the O atom attached to the metal is the electrophile and the oxygen atom on the incoming water molecule is the nucleophile. For a bond to form, it is anticipated that there needs to be orbital overlap between the highest occupied molecular orbital of the nucleophile and the lowest unoccupied molecular orbital of the electrophile. Accordingly, we might expect to observe the LUMO more strongly localized at the metal-oxygen in the most catalytically active $[M^V=O]^{3+}$complexes. To explore this concept, we investigated the LUMOs of select catalysts from our series. Some of the Fe catalysts exhibited this character, but they did not clearly correlate with lower energy barrier differences. In fact, the LUMO for the $[Fe^V=O]^{3+}$ state mostly resided on the ligands, which contrasts with the expected model shown for some ruthenium catalysts [18]. Additionally, even some energetically favorable Fe catalysts showed LUMO orbital character almost exclusively on the ligands while corresponding Ru catalysts displayed more Ru-O highlighted in the LUMO (Figure 6). This may suggest an alternate mechanism would compete in Fe catalysts. However, we found that the metal oxygen bond lengthens for all catalysts from $[M^V-O]^{3+}$ to the product $[M^{III}-OOH]^{2+}$, which follows the originally proposed mononuclear ruthenium water oxidation mechanism as O-O bond forming weakens the M-O bond. All in all, our molecular orbital exploration allows us to qualitatively observe some similarities between Ru and Fe catalysts but not surprisingly indicate that designing a robust and highly effective Fe mononuclear catalyst will be more of a challenge. The HOMO and LUMO localization and behavior are strongly influenced by the particular ligands with every catalyst exhibiting unique features.
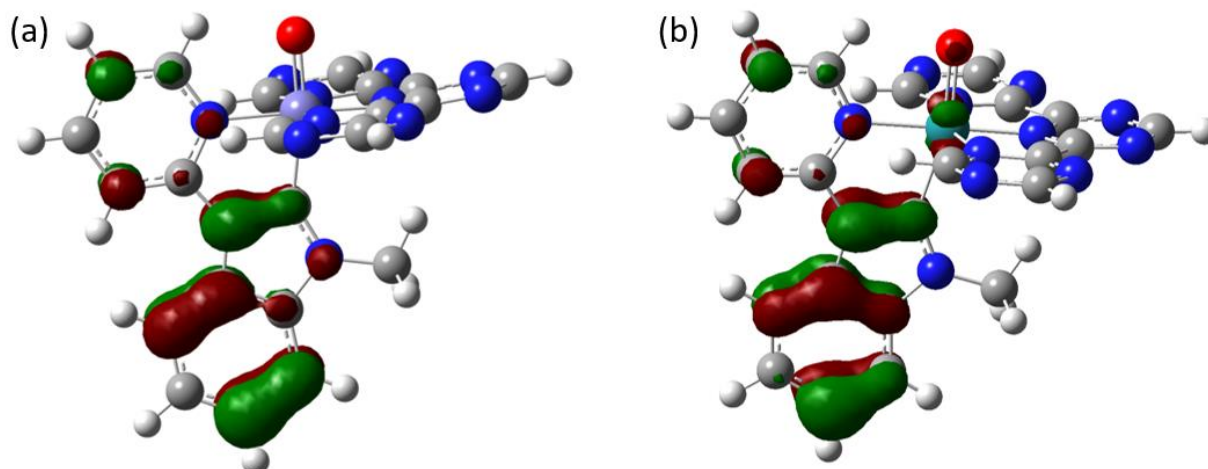
Figure 6. Iso-surface plots of the LUMO for catalyst 19 with (a) showing the LUMO for the $[Fe^V=O]^{3+}$ state of the catalyst where the subsequent ΔG ($k_{o\text{-}o}$) = 11.4 kcal/mol, while (b) displays the corresponding $[Ru^V=O]^{3+}$ with some character on the Ru-O despite the slightly less favorable ΔG ($k_{o\text{-}o}$) of 12.9 kcal/mol following this state. (The iso-surface value for these plots was set to 0.05.)

4. Conclusions

Understanding underlying principles that balance the competing concerns across the mechanistic steps of a water oxidation mechanism is important for developing efficient, robust, and sustainable water oxidation catalysts. Our computational study comparing mononuclear iron with ruthenium across 20 catalysts with varying tridentate and/or bidentate ligands displays significant impact on energetics at the critical mechanistic steps and helps elucidate some of these design challenges. We observe some common trends between ruthenium and iron WOCs when characterizing the energetics at each electrochemical step leading to the $[M^V=O]^{3+}$ oxidation state followed by the oxygen-oxygen bond formation as well as the associated intramolecular features at key steps. Iron and ruthenium catalysts generally show similar energetic trends and behavior with ruthenium broadly exhibiting lower redox potentials and energy barriers for the O-O formation step compared with iron. The only exception was catalyst 19 ([Fe(ttz)(Mebim-py)(OH$_2$)]$^{2+}$), which demonstrates more favorable energetics than its Ru counterpart. By investigating changes in 'active site' bond length (Fe-O) and Mulliken charges for the Fe catalysts, we show that ligand choice strongly influences the nature of the $[Fe^V=O]^{3+}$ complex. Catalysts with high redox potentials correlate with larger differences in Fe-O bond length and/or Mulliken charge on both the Fe and O atomic positions. Qualitatively investigating the LUMO at the $[M^V=O]^{3+}$ oxidation state reveals that ligand choice leads to distinct molecular orbital character for each catalyst and also hints at challenges in designing the more sustainable iron catalyst relative to their ruthenium counterparts. Even with the large set of catalysts presented here, we do not observe ligands that universally lead to better working catalysts at all steps along the mechanism. This again highlights the trend showing competition between the M(V/IV) redox step and O-O bond forming step. Although the energetics are not anticipated to correspond directly between our computational approach relative to experimental measurements, we hope that the trends are instructive in catalyst design principles. Additionally, computational investigation provides a complementary view of WOCs that can pinpoint why a given catalyst appears inactive experimentally. Our study provides some encouragement that mononuclear iron catalysts with appropriate ligand choice may mimic the basic features of mononuclear ruthenium catalysts for water oxidation while doing so more sustainably. We are hopeful that with further experimental and computational studies, more optimal catalysts will be explored and synthesized.

Acknowledgments

collaborators particularly Kelly Hunter, Emmett Barnes, Daniel Bhatt, Madison Doty, Hyeyoung Kim, Paul DongWoo Chang, Juan Melendez, and Kevin Joerger over the course of this study.

Conflict of interest

There is no conflict of interest for this study.

References

[1] Oni AO, Anaya K, Giwa T, Di Lullo G, Kumar A. Comparative assessment of blue hydrogen from steam methane reforming, autothermal reforming, and natural gas decomposition technologies for natural gas-producing regions. *Energy Conversion and Management*. 2022; 254:115245. https://doi.org/10.1016/j.enconman.2022.115245

[2] Umena Y, Kawakami K, Shen JR, Kamiya N. Crystal structure of oxygen-evolving photosystem II at a resolution of 1.9 Å. *Nature*. 2011; 473(7345): 55-60. https://doi.org/10.1038/nature09913

[3] Nocera DG. The artificial leaf. *Acc Chem Res*. 2012; 45(5): 767-76. https://doi.org/10.1021/ar2003013

[4] Krewald V, Retegan M, Cox N, Messinger J, Lubitz W, DeBeer S, Neese F, Pantazis DA. Metal oxidation states in biological water splitting. *Chem Sci*. 2015; 6(3): 1676-95. https://doi.org/10.1039%2Fc4sc03720k

[5] Wang N, Zheng H, Zhang W, Cao R. Mononuclear first-row transition-metal complexes as molecular catalysts for water oxidation. *Chinese Journal of Catalysis*. 2018; 39(2): 228-44. http://dx.doi.org/10.1016/S1872-2067(17)63001-8

[6] Ellis WC, McDaniel ND, Bernhard S, Collins TJ. Fast Water Oxidation Using Iron. *Journal of the American Chemical Society*. 2010; 132(32): 10990-1. https://doi.org/10.1021/ja104766z

[7] Fillol JL, Codolà Z, Garcia-Bosch I, Gómez L, Pla JJ, Costas M. Efficient water oxidation catalysts based on readily available iron coordination complexes. *Nat Chem*. 2011; 3(10): 807-13. https://doi.org/10.1038/nchem.1140

[8] Coggins MK, Zhang M-T, Vannucci AK, Dares CJ, Meyer TJ. Electrocatalytic Water Oxidation by a Monomeric Amidate-Ligated Fe(III)–Aqua Complex. *Journal of the American Chemical Society*. 2014; 136(15): 5531-4. https://doi.org/10.1021/ja412822u

[9] Jarvis EAA, Lee B, Neddenriep B, Shoemaker W. Computational comparison of stepwise oxidation and O–O bond formation in mononuclear ruthenium water oxidation catalysts. *Chemical Physics*. 2013; 417: 8-16. https://doi.org/10.1016/j.chemphys.2013.03.007

[10] Chen Z, Concepcion JJ, Luo H, Hull JF, Paul A, Meyer TJ. Nonaqueous Catalytic Water Oxidation. *Journal of the American Chemical Society*. 2010; 132(50): 17670-3. https://doi.org/10.1021/ja107347n

[11] Wang L, Wang L. Ligands modification strategies for mononuclear water splitting catalysts. *Front Chem*. 2022; 10:996383. https://doi.org/10.3389/fchem.2022.996383

[12] Becke AD. Density-functional thermochemistry. III. The role of exact exchange. *Journal of Chemical Physics*. 1993; 98: 5648-52. https://doi.org/10.1063/1.464913

[13] Hay PJ, Wadt WR. *Ab initio* effective core potentials for molecular calculations. Potentials for K to Au including the outermost core orbitals. *Journal of Chemical Physics*. 1985; 82: 299-310. https://doi.org/10.1063/1.448975

[14] Cances E, Mennucci B, Tomasi J. A new integral equation formalism for the polarizable continuum model: Theoretical background and applications to isotropic and anisotropic dielectrics *Journal of Chemical Physics*. 1997; 107(8): 3032-41. http://link.aip.org/link/doi/10.1063/1.474659?ver=pdfcov

[15] Scalmani G, Frisch MJ. Continuous surface charge polarizable continuum models of solvation. I. General formalism. *Journal of Chemical Physics*. 2010; 132: 114110-1-15. https://doi.org/10.1063/1.3359469

[16] Gaussian 16, Revision C.01, Frisch MJ, Trucks GW, Schlegel HB, Scuseria GE, Robb MA, Cheeseman JR, Scalmani G, Barone V, Petersson GA, Nakatsuji H, Li X, Caricato M, Marenich AV, Bloino J, Janesko BG, Gomperts R, Mennucci B, Hratchian HP, Ortiz JV, Izmaylov AF, Sonnenberg JL, Williams-Young D, Ding F, Lipparini F, Egidi F, Goings J, Peng B, Petrone A, Henderson T, Ranasinghe D, Zakrzewski VG, Gao J, Rega N, Zheng G, Liang W, Hada M, Ehara M, Toyota K, Fukuda R, Hasegawa J, Ishida M, Nakajima T, Honda Y, Kitao O, Nakai H, Vreven T, Throssell K, Montgomery JA Jr, Peralta JE, Ogliaro F, Bearpark MJ, Heyd JJ, Brothers EN, Kudin KN, Staroverov VN, Keith TA, Kobayashi R, Normand J, Raghavachari K,

Rendell AP, Burant JC, Iyengar SS, Tomasi J, Cossi M, Millam JM, Klene M, Adamo C, Cammi R, Ochterski JW, Martin RL, Morokuma K, Farkas O, Foresman JB, Fox DJ. Gaussian, Inc., Wallingford CT, 2016.

[17] Mulliken RS. Electronic population analysis on LCAO-MO molecular wave functions. *Journal of Chemical Physics*. 1955; 23: 1833-40. http://dx.doi.org/10.1063/1.1740588

[18] Wang LP, Wu Q, Van Voorhis T. Acid− base mechanism for ruthenium water oxidation catalysts. *Inorganic chemistry*. 2010; 49(10): 4543-53. https://doi.org/10.1021/ic100075k

[19] Wang LP, Van Voohris T. A polarizable QM/MM explicit solvent model for computational electrochemistry in water. *Journal of Chemical Theory and Computation*. 2012; 8: 610-7. https://doi.org/10.1021/ct200340x

[20] Tissandier MD, Cowen KA, Feng WY, Gundlach E, Cohen MH, Earhart AD, Coe JV, Tuttle TR. The proton's absolute aqueous enthalpy and Gibbs free energy of solvation from cluster-ion solvation data. *Journal of Physical Chemistry A*. 1998; 102(40): 7787-94. https://doi.org/10.1021/jp982638r

[21] Chen Z, Concepcion JJ, Hu X, Yang W, Hoertz PG, Meyer TJ. Concerted O atom-proton transfer in the O-O bond forming step in water oxidation. *Proceedings of the National Academy of Sciences*. 2010; 107(16): 7225-9. https://doi.org/10.1073/pnas.1001132107

[22] Watabe S, Tanahashi Y, Hirahara M, Yamazaki H, Takahashi K, Mohamed EA, Tsubonouchi Y, Zahran ZN, Saito K, Yui T, Yagi M. T. Critical Hammett Electron-Donating Ability of Substituent Groups for Efficient Water Oxidation Catalysis by Mononuclear Ruthenium Aquo Complexes. *Inorganic Chemistry*. 2019; 58(19): 12716-23. https://doi.org/10.1021/acs.inorgchem.9b01623

[23] Privalov T, Åkermark B, Sun L. The O-O Bonding in Water Oxidation: the Electronic Structure Portrayal of a Concerted Oxygen Atom–Proton Transfer Pathway. *Chemistry – A European Journal*. 2011; 17(30):8313-7. https://doi.org/10.1002/chem.201100901